Materials Advances

ROYAL SOCIETY OF CHEMISTRY

PAPER

View Article Online
View Journal | View Issue

Cite this: *Mater. Adv.*, 2024, 5, 8909

Role of intermolecular charge transfer towards fluorometric detection of fluoride ions with anthrapyrazolone derivatives†

Gomathi Sivakumar, Anashwara Babu, Anubhab Das, Mageshwari Anandhan, Venkatramaiah Nutalapati * and Samarendra Maji *

Received 22nd July 2024,
Accepted 6th October 2024

DOI: 10.1039/d4ma00738g

rsc.li/materials-advances

Anion detection using small molecules as chemosensors holds significant importance in the biological and environmental fields, offering several advantages over conventional methods. In this report, we have developed three anthrapyrazolone derivatives, namely 2,7-dihydrobenzo[1,2,3-*cd*:4,5,6-*c*′*d*′]bis(indazole) (**DHBBI**), 2-(benzo[1,2,3-*cd*:4,5,6-*c*′]bis(indazole)-2(7*H*)-yl)ethanol (**DHBBI-OH**), and 2,2′-(benzo[1,2,3-*cd*:4,5,6-*c*′*d*′]bis(indazole)-2,7-diyl)diethanol (**DHBBI-2-OH**), utilizing straightforward chemical reactions. These compounds were investigated for the fluorometric detection of a series of anions *viz.* F^-, Cl^-, Br^-, I^-, OH^-, CN^-, ClO_4^-, SO_4^{2-}, NO_3^- and SCN^- in the form of tetrabutylammonium salts. Detailed photophysical and mechanistic investigations were conducted to understand the interactions of three fluorophores with different anions. Fluorescence analysis showed considerable changes in the emission intensity of the three fluorophores in the presence of a series of anions as mentioned earlier. Among the synthesized molecules, **DHBBI** (K_{sv} = 11.6 × 10^4 M^{-1}) exhibited the highest selectivity with ∼1.30 and 1.80 fold higher association rate constants and sensitivity with a limit of detection of ∼10.3 mM towards F^- ions compared to **DHBBI-OH** and **DHBBI-2-OH**. The selectivity and sensitivity towards F^- ions were demonstrated in light of hydrogen-bonding interactions between **DHBBI** and F^- ions. Additionally, DFT and TDDFT studies were employed for **DHBBI** and its derivatives to investigate their structural insights and electronic properties comprehensively.

1. Introduction

The interest in creating new, compact, and efficient compounds for precise qualitative and quantitative anion detection as chemical sensors is growing rapidly.[1–7] Research on novel chemosensors for anion detection through hydrogen bond interactions[8] has been an active topic due to the significance of anions in a wide range of therapeutic,[4,9,10] environmental,[11–13] and biological activities.[14–16] Much of the research has focused on optical sensors for anions, which detect changes in colour or fluorescence intensity.[17,18] Additionally, these sensors using the spectroscopic technique for monitoring anions have several benefits, including high selectivity, sensitivity and real-time monitoring, and provide detailed molecular information. These devices are easy to use and have acquired attention for the above reasons.[19,20] Despite being sensitive to environmental factors, their versatility and non-destructive nature make them essential in scientific and industrial applications. Consequently, selective anion detection using these methods is vital. The ability of spectroscopic methods to detect multiple analytes offers significant advantages over other sensing techniques, such as electrochemical analysis, capillary electrophoresis, and high-performance liquid chromatography (HPLC), due to its rapid response and simplicity.[21–26]

Fluoride ions (F^-), despite their small size, have significant biological roles, including in dental health and osteoporosis treatment, but they can also cause environmental and health risks.[27–32] Additionally, F^- is a crucial mineral for the proper growth, development, and maintenance of healthy hair, nails, teeth, and bones. Sodium fluoride (NaF) is a component of toothpaste and plays a vital role in promoting body growth. A F^- concentration of 0.5 to 1.0 ppm in drinking water is believed to be effective for promoting metabolism. Whereas, high amounts of F^- can result in environmental damage and give rise to diseases such as dental or skeletal fluorosis, nephrotoxic consequences and urolithiasis in human beings. Moreover, there is a correlation between F^- toxicity with enhanced bone density, elevated risks of cancer, gastrointestinal problems,

Department of Chemistry, Faculty of Engineering and Technology, SRM Institute of Science and Technology (SRMIST), Kattankulathur, Tamil Nadu-603203, India. E-mail: nvenkat83@gmail.com, venkatrv1@srmist.edu.in, samarenr@srmist.edu.in

† Electronic supplementary information (ESI) available: ^{1}H NMR, ESI MS, DFT, fluorescence studies, and UV-vis studies. See DOI: https://doi.org/10.1039/d4ma00738g

and kidney damage.[33,34] Hence, it is important to identify the presence of hazardous levels of F^- using a straightforward approach and take appropriate measures to reduce the potential risks to both human health and the environment.[35]

Recently, fluorophores have been designed and reported as colorimetric and fluorometric anion sensors. These sensors utilize various signalling blocks, such as anthracene,[36,37] dansyl[38,39] imidazole,[40,41] anthraquinone,[42,43] indole,[44,45] nitrobenzene azo groups,[46,47] and other conjugated moieties,[48] which are covalently connected to anion receptors.

Yadav and his team developed 1,8-naphthalimide-derived chromo-fluorogenic chemosensors to detect F^- ions, with detection limits of 1.34 nM.[49] Li *et al.* designed boronic acid-pyrene derived carbon dot-based fluorophores and used them to sense F^- with LOD of 5.9×10^{-5} M.[50] Wu *et al.* developed 4-(2,2-dichloroacetamide)-*N*-*n*-butyl-naphthalimide and 1,8-naphthalimide (CNA) probes to detect F^- ions using colorimetric and fluorescence methods. The CNA was able to identify F^- with LODs of 0.52 μM from fluorescence spectra and 1.41 μM from ratiometric absorption spectra.[51]

Besides the widely used fluorophore molecules mentioned above, anthrapyrazolone stands out as a significant organic fluorophore due to its remarkable properties, such as intense fluorescence emission in the visible range, high photostability, and exceptional sensitivity for analyte detection.[52,53] These properties make it highly suitable for sensor applications, particularly in biological samples and environmental pollutant monitoring. Its versatility has led to widespread use in the design of synthetic structures and materials. Prasad and his coworkers studied the use of a small fluorescent molecule, 1,9-pyrazoloanthrone, as a ''*turn-on*'' fluorescence probe for the detection of CN^- and F^- ions. Although this molecule has primarily been employed as an inhibitor for c-JUN N-terminal kinase (JNK1/2), its potential in ion detection was highlighted and demonstrated selective fluorometric detection towards CN^- and F^- ions among seven anions.[52] Maji *et al.* conducted a study using copolymer and 1,9-pyrazoloanthrone derivatives to detect 2,4,6-trinitrophenol with a LOD of ~83 μM.[53] In addition to this study, the same group designed an anthrapyrazolone derivative named 2-(benzo[1,2,3-*cd*:4,5,6-*c*′*d*′]bis-(indazole)-2(7*H*)-yl)ethyl methacrylate (**DHBBI**-MA) specifically for the detection of SCN^- and F^- ions.[54] To the best of our knowledge, there have been few reports of a single molecular probe capable of selectively detecting and distinguishing single anionic species.

Thus, herein this study, we have synthesized and characterized anthrapyrazolone-based molecules: 2,7-dihydrobenzo [1,2,3-*cd*:4,5,6-*c*′*d*′]bis(indazole) (**DHBBI**), 2-(benzo[1,2,3-*cd*:4,5,6-*c*′]bis(indazole)-2(7*H*)-yl)ethanol (**DHBBI-OH**), and 2,2′-(benzo-[1,2,3-*cd*:4,5,6-*c*′*d*′]bis(indazole)-2,7-diyl)diethanol (**DHBBI-2-OH**), and thoroughly examined their mechanism of molecular interactions with F^- anions. The impact of increasing the number of hydroxyalkyl units in anthrapyrazolone derivatives on the F^- anion's selectivity and sensitivity was investigated using fluorescence methods to determine the effect of hydrogen bonding interaction with the hydroxyl group that may influence the detection. Interference analysis with various other anions was demonstrated for the selectivity of **DHBBI**. Computational analysis using the DFT method provided insight into the electronic characteristics of molecular hydrogen bonding that support the experimental observations.

2. Materials and methods

2.1. Materials

All solvents and chemicals utilized in this study were of analytical grade and used without further purification. 1,5-Dichloroanthraquinone and hydroquinone were obtained from Sigma Aldrich with purity >98%, while 2-bromoethanol (>97% Purity) was procured from TCI Chemicals (India) *Pvt. Ltd.* Pyridine (98% purity) and sodium acetate (CH_3COONa) (97% purity) were obtained from Lobachemie *Pvt. Ltd.* India. Hydrazine monohydrate (>98.0% purity), triethylamine (TEA) (99% purity), *N*,*N*-dimethylformamide (DMF), dichloromethane (DCM), ethyl acetate (EA), methanol, and hexane were supplied by Finar Chemicals Limited, India. Additionally, 4-dimethylaminopyridine (DMAP), potassium carbonate (K_2CO_3) with >99.0% purity, and acetonitrile (ACN) were acquired from Sisco Research Laboratories *Pvt. Ltd*. (SRL), India. All these solvents were distilled prior to use in reactions.

2.2. Characterization

The UV-vis absorption spectra for **DHBBI**, **DHBBI-OH**, and **DHBBI-2-OH** were measured in acetonitrile (ACN) using an Agilent Cary 60 UV-vis spectrophotometer. Fourier transform infrared (FT-IR) spectra were analyzed within the 4000–400 cm^{-1} range using a Shimadzu IRTracer-100 FT-IR spectrometer. ^{1}H-NMR spectra were obtained using Bruker 500 MHz NMR spectrometers with DMSO-d_6 as the solvent. The ESI-MS spectra of **DHBBI**, **DHBBI-OH**, and **DHBBI-2-OH** were characterized using an Agilent 6230B Time-of-Flight (TOF) mass spectrometer. The Edinburgh FLS-1000 spectrofluorometer was used for room-temperature fluorescence investigations. Fluorescence lifetime decay in ACN was measured using a 380 nm LED and a 450 nm diode laser as the excitation source. A cuvette was filled with a solution of 3.0 mL **DHBBI** and its derivatives (10 μM), and the preliminary emission was obtained with 400 nm excitation. An aliquot of 10 μL of analyte solution prepared in ACN was added to the cuvette. Following every addition of the analyte, the cuvette was closed and thoroughly stirred, and a fluorescence spectrum was recorded. This method was continued with different analyte concentrations to get significant fluorescence quenching. The Stern–Volmer equation (eqn (1)) was then used to determine the Stern–Volmer association rate constants (K_{sv}).

$$I_0/I = 1 + K_{sv}[Q] \quad (1)$$

where I_0 and I are the fluorescence intensities before and after analyte addition, respectively, K_{sv} is the Stern–Volmer constant, and [Q] is the analyte concentration. Quenching efficiency and fluorescence emission spectra were examined, and interference from various analytes was similarly investigated.

Computational analyses were performed using Gaussian 09 and Gauss View 6.0 for visualization. Ground and excited states were optimized using density functional theory (DFT) and time-dependent DFT (TDDFT) methods with a B3LYP/6-31g* basis set. The interaction energy of **DHBBI** with anions was calculated using the following equations (eqn (2)):

$$E_{int} = E_{complex} - (E_{compound} + E_{anion}) \quad (2)$$

$E_{complex}$ is the energy of the complex formed between **DHBBI** and the anion, whereas $E_{compound}$ and E_{anion} are the energies of the isolated **DHBBI** and anion, respectively. Cyclic voltammetry (CV) was conducted using a BioLogic VSP 300 with a three-electrode setup in ACN with a supporting electrolyte. The working electrode was glassy carbon (GC), with platinum as a counter electrode, and a non-aqueous Ag/Ag^+ electrode acted as a reference electrode. Ferrocene was used as an internal standard, and tetrabutylammonium hexafluorophosphate (NBu_4PF_6) (0.1 M) was the supporting electrolyte. CV characteristic studies were measured at scan rates ranging from 20 mV s^{-1} to 100 mV s^{-1} under standard conditions of 25.0 ± 0.1 °C to analyse the electrochemical behaviour of the molecules.

2.3. Synthesis of 2,7-dihydrobenzo[1,2,3-*cd*:4,5,6-*c′d′*]bis(indazole) [DHBBI]

The **DHBBI** molecule was synthesized using the method outlined in the literature (Scheme 1).[54] In a 250 mL round-bottom flask, 5.0 g (18 mmol) of 1,5-dichloroanthraquinone and 3.6 g (43 mmol) of sodium acetate were combined with 25 mL of pyridine. To this mixture, 6 mL of hydrazine monohydrate was added, and the reaction was refluxed at 120 °C for 24 h under a nitrogen atmosphere. The progress of the reaction was monitored by thin-layer chromatography (TLC). Vacuum distillation was used to extract the pyridine once the reaction was complete. The crude product was then purified using column chromatography with a 70 : 30 solvent mixture of dichloromethane (DCM) and ethyl acetate (EA). Finally, pure 2,7-dihydrobenzo[1,2,3-*cd*:4,5,6-*c′d′*]bis(indazole) (**DHBBI**) was obtained by removing the solvents under reduced pressure, yielding 3.1 g (74%). ^{1}H NMR (500 MHz, DMSO-d_6) δ (ppm): 13.149 (s, 2H), 7.47–7.37 (m, 6H). ESI-MS calculated for $C_{14}H_8N_4$: 232.07, found: m/z = 233.05 $[M + H]^+$.

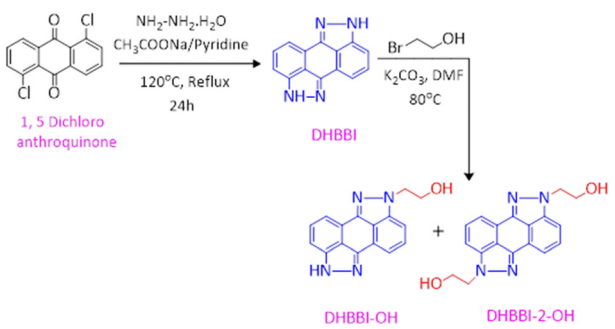

Scheme 1 Schematic representation for the synthesis of **DHBBI**, **DHBBI-OH**, and **DHBBI-2-OH**.

2.4. Synthesis of 2-(benzo[1,2,3-*cd*: 4,5,6-*c′d′*]bis(indazole)-2(7*H*)-yl)ethanol [DHBBI-OH] and 2,2′-(benzo[1,2,3-*cd*:4,5,6-*c′d′*]bis(indazole)-2,7-diyl)diethanol [DHBBI-2-OH]

These compounds were synthesized following a procedure from the literature.[54] The reaction involved treating 1.94 g (8.35 mmol) of dihydrobenzoindazole with 2 mL of 2-bromoethanol in the presence of anhydrous K_2CO_3 (3.5 g, 25 mmol) using dimethylformamide (DMF) as the solvent. The mixture was heated to 80 °C under N_2 conditions (Scheme 1). TLC was used to monitor the reaction, revealing the formation of mono- and di-substituted ethanol derivatives of **DHBBI**. After completion, the DMF was removed by vacuum distillation, and the crude products were purified by silica chromatography (60–120 mesh) using a 60 : 40% mixture of EA and DCM. The solvents were then evaporated under reduced pressure to yield **DHBBI-OH** (1.2 g, 37.5%) with ^{1}H NMR (500 MHz, DMSO-d_6) δ (ppm): 13.19 (s, 1H), 7.51–7.40 (m, 6H), 4.97 (t, J = 5.1 Hz, 1H), 4.50 (t, J = 5.4 Hz, 2H), 3.89 (q, J = 5.6 Hz, 2H). ESI-MS calculated for $C_{16}H_{12}N_4O$: 276.10, found: m/z = 277.15 $[M + H]^+$, and **DHBBI-2-OH** (0.520 g, 15.6%) with ^{1}H NMR (500 MHz, DMSO-d_6) δ (ppm): 7.53–7.44 (m, 6H), 4.9 (t, J = 4.75 Hz, 2H), 4.490 (t, J = 5.45 Hz, 4H), 3.89 (q, J = 5.5 Hz, 4H) and ESI-MS calculated for $C_{18}H_{16}N_4O_2$: 320.13, found: m/z = 320 $[M]^+$.

3. Results and discussion

3.1. Synthesis and characterization of, DHBBI, DHBBI-OH, and DHBBI-2-OH

In the current study, three fluorophore molecules, **DHBBI**, **DHBBI-OH**, and **DHBBI-2-OH** were synthesized. To prepare **DHBBI**, 1,5-dichloroanthraquinone, and hydrazine monohydrate were initially subjected to a condensation process with pyridine and sodium acetate at 120 °C for 24 hours. This process yielded 74% after isolation (Scheme 1). **DHBBI-OH** and **DHBBI-2-OH** were produced by reacting **DHBBI** with 2-bromoethanol at 80 °C in the presence of anhydrous K_2CO_3. ^{1}H NMR, FT-IR, and mass spectrometry confirmed the chemical structures of the compounds.

The ^{1}H NMR spectrum of **DHBBI** (Fig. S1, ESI†) shows that six aromatic protons appear in the region of δ 7.48–7.38 ppm and the signal at δ 13.19 ppm corresponds to the –NH proton in the indazole moiety. This reveals that 1,5-dichloroanthraquinone condensed with hydrazine hydrate and formed 2,7-dihydrobenzo[1,2,3-*cd*:4,5,6-*c′d′*]bis(indazole). ESI-MS results show that the molecular ion peak at m/z 233.05 $[M + H]^+$ validates the formation of the desired **DHBBI** (Fig. S2, ESI†). The ^{1}H NMR spectrum of **DHBBI-OH** and **DHBBI-2-OH** (Fig. S3 and S4, ESI†) shows two new signals observed at δ 3.89 and δ 4.50 ppm with the coupling constants of J = 5.6 Hz and J = 5.4 Hz due to the substitution of two methylene moieties. The signal at δ 3.89 ppm is due to the presence of a $-CH_2$ proton attached to the –OH functional group, and the peak at δ 4.50 ppm is owing to methylene protons linked to the aromatic unit. In addition, the peak around δ 4.97 ppm represents the hydroxyl group from the 2-bromoethanol. The mono-substituted

DHBBI-OH was further confirmed by one –NH proton in the aromatic unit (Fig. S3, ESI†). The ESI-MS result of the molecular ion peak at *m*/*z* 277.15 $[M + H]^+$ indicates the formation of the expected compound (Fig. S5, ESI†). Similarly, the ^{1}H NMR spectrum of **DHBBI-2-OH** was also further confirmed due to the absence of the aromatic –NH group, which shows the bi-functionalization of 2-bromoethanol on the **DHBBI** molecules (Fig. S4, ESI†). The ESI-MS result of bi-functionalized **DHBBI-2-OH** exhibits the molecular ion peak at *m*/*z* 320.0 $[M]^+$ indicating the formation of the expected compound (Fig. S6, ESI†).

The FTIR spectrum of **DHBBI** showed a characteristic stretching vibration that appeared at 3028 cm^{-1} due to –NH stretching. Two stretching vibrations at 1660 cm^{-1} and 1057 cm^{-1} were attributable to C=N stretching and C–N bending vibrations (Fig. S7a, ESI†). The FTIR spectra of **DHBBI-OH** and **DHBBI-2-OH** are shown in Fig. S7b and c (ESI†) respectively.

In these spectra, a stretching vibration at 3114 cm^{-1} and a bending vibration at 1440 cm^{-1} are observed as a result of the O–H stretching and bending vibrations of the –OH group attached to the alkyl chain. An aromatic N–H stretching vibration appears at 3329 cm^{-1}, and an aliphatic C–H stretching vibration is observed at 2861 cm^{-1}. The C–O and C–N stretching vibrations appear at 1321 cm^{-1} and 1032 cm^{-1}, respectively, while a medium-poor stretching vibration at 767 cm^{-1} is corresponding to C=C bending. The FTIR spectrum of **DHBBI-2-OH** shows all the peaks present in **DHBBI-OH**, but with improved intensity.

The photophysical properties of the **DHBBI**, **DHBBI-OH**, and **DHBBI-2-OH** were analyzed through UV-visible and fluorescence spectroscopy in an ACN medium. The **DHBBI** exhibits a wide absorption band at 299 ± 2 nm due to the π → π* transition together with a small absorption band at 369.63 ± 2 and 388.7 ± 2 nm owing to the intramolecular charge transfer transition (Fig. 1a). The UV-vis absorption spectra of **DHBBI-OH** and **DHBBI-2-OH** show short broad bands at 300 nm and 307 nm, respectively, with highly intense vibronic absorption bands at 360, 377, and 400 nm for **DHBBI-OH** and 367, 386, and 408 nm for **DHBBI-2-OH**. In the case of **DHBBI-OH** and **DHBBI-2-OH**, the absorption bands are primarily attributed to the π → π* and n → π* transition. All three molecules show a similar absorption pattern in ACN with minimal variations in the absorption values that depend on the ethanol side chains on **DHBBI**. In **DHBBI**, the electron density is primarily localized on the π-conjugated anthrapyrazolone moiety. When hydroxyalkyl groups are added to form **DHBBI-OH** and **DHBBI-2-OH**, this electron density extends the anthrapyrazolone moiety to the hydroxyalkyl groups. This extension causes a redshift in the intramolecular charge transfer band. The significant redshift in the absorption spectrum of **DHBBI-OH** and **DHBBI-2-OH** compared to **DHBBI** suggests a highly planar molecular backbone with electron density concentrated on the anthrapyrazolone moiety.[55] These findings are further validated by DFT and TDDFT studies. Fig. 1b displays the fluorescence spectra of three molecules upon excitation at λ_{ex} = 368 nm. **DHBBI** exhibits emission bands at 391 nm, 414 nm, and 439 nm. The emission spectrum of **DHBBI-OH** shows highly intense emission bands at 403, 425 nm, and 451 nm. Similarly, the **DHBBI-2-OH** molecule shows intense emission bands at 410 nm, 435 nm, and 461 nm. All **DHBBI** derivatives exhibit an intense blue emission in the ACN solvent with a Stokes shift of 50 ± 20 nm. The obtained emission spectra of all **DHBBI** derivatives are independent of the excitation wavelength, resulting in emission from the $S_1 \rightarrow S_0$ state. Like the absorption spectra, the emission spectra also exhibited a red shift from **DHBBI** to **DHBBI-2-OH**. Strong intramolecular interactions in **DHBBI** derivatives cause a red shift in the emission wavelength.

The optimized geometries of all studied molecules (**DHBBI**, **DHBBI-OH**, **DHBBI-2-OH**) were obtained using the B3LYP/6-31g* method in the Gaussian 09 suite of programs and as shown in Fig. 2a. The selected bond lengths, bond angles, and dihedral angles of the designed compounds are listed in Table S1 (ESI†). The optimized structures of **DHBBI**, **DHBBI-OH**, and **DHBBI-2-OH** are almost planar. Furthermore, the frontier molecular orbitals of **DHBBI** and its derivatives showed that the electron density of both the HOMO and LUMO was

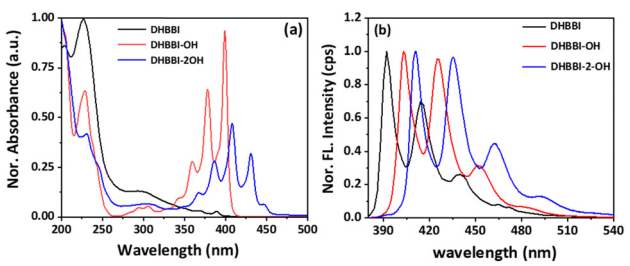

Fig. 1 (a) UV-visible and (b) fluorescence emission spectra of **DHBBI**, **DHBBI-OH**, and **DHBBI-2-OH** in ACN solution.

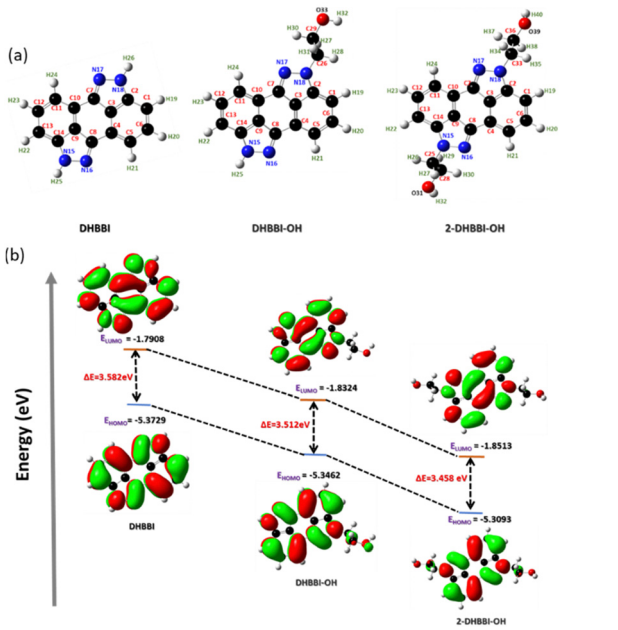

Fig. 2 (a) Optimized geometry and (b) energy profile diagram of **DHBBI**, **DHBBI-OH**, and **DHBBI-2-OH** obtained using DFT/B3LYP/6-31g*.

predominantly localized on the entire π-conjugated anthrapyrazolone moiety. The HOMO–LUMO energy levels, electron density distribution, and band gap for the **DHBBI**, **DHBBI-OH**, and **DHBBI-2-OH** were calculated. The HOMO and LUMO energy levels of **DHBBI** are −5.37 eV and −1.79 eV, respectively, with an estimated band gap of 3.58 eV (Fig. 2b). Functionalization with 2-bromoethanol (**DHBBI-OH** and **DHBBI-2-OH**) decreases the HOMO–LUMO energy gap, resulting in band gaps of 3.51 eV for **DHBBI-OH** and 3.45 eV for **DHBBI-2-OH**. Both mono and di-substituted derivatives exhibit the same electronic structures, although the energy levels are lower due to functionalization. The HOMO electron density of **DHBBI** is located on the π-conjugated anthrapyrazolone moiety, while in the case of **DHBBI-OH** and **DHBBI-2-OH**, it extends to the functionalized ethanol units. The LUMO electron density remains primarily on the central core, indicating a charge transfer process similar to **DHBBI**.

Molecules with higher oxidation potential have a greater tendency to lose electrons and be oxidized. Similarly, the oxidation potentials of **DHBBI** are higher due to increased electron density in its donor unit, as confirmed by cyclic voltammetry (Fig. 3). The onset oxidation potentials follow the order: **DHBBI** (1.01 V) > **DHBBI-OH** (0.97 V) > **DHBBI-2-OH** (0.93 V). All three molecules exhibit reversible oxidation and reduction peaks. The HOMO and LUMO energy levels, as well as the bandgaps from CV and DFT, are summarized in Table 1. All the **DHBBI** derivatives exhibit low-lying HOMO energy levels, with **DHBBI** showing the lowest HOMO energy level, as calculated from its oxidation potential peak position.

The LUMO energies calculated from reduction potential indicate that the addition of hydroxyalkyl units to **DHBBI** results in a notable decrease in the energy levels of **DHBBI-OH** and **DHBBI-2-OH**. This reduction is more significant than that predicted by DFT calculations. Functionalization (**DHBBI-OH**, **DHBBI-2-OH**) results in lower HOMO energies and smaller band gaps compared to **DHBBI**. The frontier orbital energies of these D–π–A systems are suitable for hole and electron injection, enhancing their optoelectronic functionality. The band gap calculated from electrochemical measurements was almost similar to the DFT band gap (Fig. 3 and Table 1).

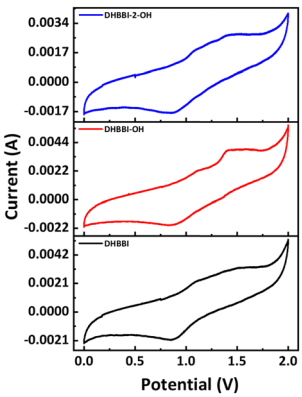

Fig. 3 Cyclic-voltammograms of **DHBBI**, **DHBBI-OH**, and **DHBBI-2-OH**.

Table 1 Electrochemical and DFT data of **DHBBI**, **DHBBI-OH**, and **DHBBI-2-OH**

	Electrochemical				DFT
Complex	$E_{ox,onset}$ [a] (V)	$E_{red,onset}$ [b] (V)	E_{HOMO}/E_{LUMO} [d] (eV)	$E_{g,opt}$ [c] (eV)	$E_{g,opt}$ (eV)
DHBBI	1.01	1.11	−5.81/−2.63	3.18	3.58
DHBBI-OH	0.97	1.20	−5.77/−2.67	3.10	3.51
DHBBI-2-OH	0.93	1.21	−5.73/−2.94	2.79	3.45

[a] The onset of oxidation of **DHBBI**, **DHBBI-OH**, and **DHBBI-2-OH**. [b] The onset of the reduction curves of **DHBBI**, **DHBBI-OH**, and **DHBBI-2-OH**. [c] Optical gap = $(1240/\lambda_{onset})$. [d] $E_{HOMO} = -[E_{ox.onset} + 4.8]$ eV, $E_{LUMO} = E_{HOMO} + E_g$.

Electrostatic potential (ESP) surfaces of **DHBBI**, **DHBBI-OH**, and **DHBBI-2-OH** show that the anthrapyrazolone core is an attractive site for electron donors. In **DHBBI**, N17 and N16 are highly negative. At the same time, **DHBBI-OH** and **DHBBI-2-OH** show similar regions at N15, O33, and O31, O39 indicating sites for electrophilic attack (Fig. S8a, ESI†). TD-DFT (B3LYP/6-31g*) calculations were also performed to determine the orbitals involved in the predominant excited-state electronic transitions, and their corresponding energies and oscillator strengths are summarized in Table S2 (ESI†). TD-DFT analysis indicates that the primary electronic transitions ($S_0 \rightarrow S_1$) for these three molecules are HOMO to LUMO transitions. Table S2 (ESI†) demonstrates a gradual increase in oscillator strength from **DHBBI** to **DHBBI-2-OH**. This increase is attributed to the improved electronic coupling between the donor and acceptor moieties, which aligns with our findings from optical spectroscopy. As the number of ethanolic groups on the **DHBBI** molecule increases, the low-energy transition shifts from approximately 360 nm (**DHBBI**) to 369 nm (**DHBBI-OH**) and then to 377 nm (**DHBBI-2-OH**). The differences in absorption maxima between theoretical calculations and experimental observations may be attributed to factors such as solvent molecules, which are not considered in the TD-DFT computations (Fig. S8b and Table S2, ESI†).

3.2. Detection of anions

To study the chemosensing behaviour of the **DHBBI** and its derivatives, absorption and fluorescence studies were measured in ACN solution at 25 °C. The anion sensing ability of **DHBBI**, **DHBBI-OH**, and **DHBBI-2-OH** was evaluated by spherical anions (F^-, Cl^-, Br^- and I^-), linear (OH^-, CN^-) and large ions (ClO_4^-, SO_4^{2-}, NO_3^-) in the form of tetrabutylammonium salts.

Fig. 4a–c shows a change in the emission spectra of **DHBBI**, **DHBBI-OH**, and **DHBBI-2-OH** upon the gradual incorporation of various concentrations of F^- ions. Upon the gradual addition of an F^- ion (1.7×10^{-4} M) to the **DHBBI**, **DHBBI-OH**, and **DHBBI-2-OH**, a gradual decrease in the fluorescence emission intensity was observed. The emission intensity of **DHBBI** decreased by 40% upon the addition of 167 μM of F^- ions (Fig. 4a). The emission intensity only decreased by 7–18% when other analytes were added. Fig. 4b shows that the initial intensity of the **DHBBI-OH** solution was reduced by 19% when

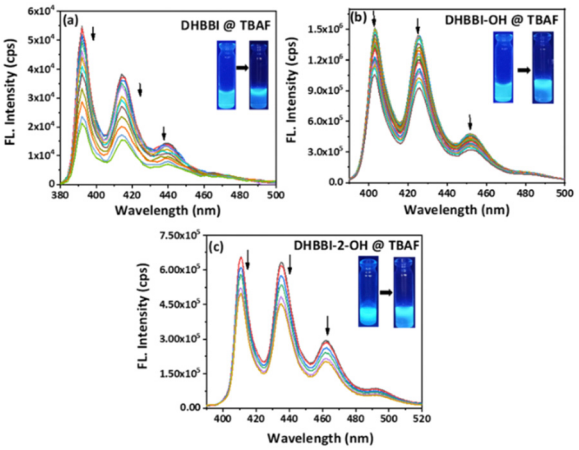

Fig. 4 Change in fluorescence emission behaviour of (a) **DHBBI**, (b) **DHBBI-OH** and (c) **DHBBI-2-OH** in ACN (7×10^{-6} M) upon addition of different concentrations of TBAF (167 μM).

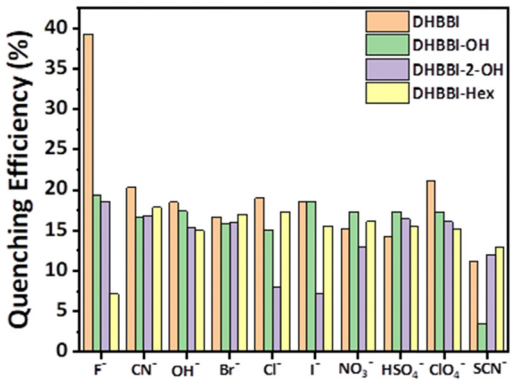

Fig. 5 Quenching efficiency of **DHBBI**, **DHBBI-OH**, **DHBBI-2-OH**, and **DHBBI**-Hex (7×10^{-6} M) treated with various anions in the form of tetrabutylammonium salts (167 μM).

167 μM of F^- anions was added. The initial fluorescence intensity of **DHBBI-2-OH** is quenched by 18% under the same conditions (Fig. 4c).

Fluorescence quenching experiments were conducted to analyse the quenching rates, the selectivity for sensing various anions, and their interactions with **DHBBI**, **DHBBI-OH**, and **DHBBI-2-OH** molecules. These studies show that **DHBBI** exhibits a superior quenching behaviour with the F^- ion than the other two derivatives in the order of **DHBBI** > **DHBBI-OH** > **DHBBI-2-OH**. Moreover, the other remaining anions (CN^-, OH^-, Cl^-, Br^- and I^-, OH^-, CN^-, ClO_4^-, SO_4^{2-}, NO_3^-, SCN^-) did not show considerable change in emission spectra. DFT and TD-DFT were used to study the binding mechanisms of F^- with **DHBBI** and its derivatives (Fig. S9, ESI†). The interaction of the optimized **DHBBI** and **DHBBI-OH** probes with the F^- ion revealed strong interaction energy between **DHBBI** and F^-, consistent with experimental findings. ESP showed a substantial reduction in electron density at the ring's centre upon complexation with F^- due to its high electronegativity. **DHBBI**@F^- displayed the most significant reduction in its electron density as observed from the ESP image (Fig. S10, ESI†). **DHBBI-OH** also showed reduced electron density with F^- (Fig. S11, ESI†), and very minimal changes were observed in the ESP map of **DHBBI-2-OH** upon anion complexation. The HOMOs and LUMOs were spread over the aromatic rings, with energy differences of 3.582 eV and 3.512 eV for **DHBBI** and **DHBBI-OH**, respectively (Fig. S12 and S13, ESI†). Anion complexation led to a significant reduction in the HOMO–LUMO energy gap, confirming intermolecular charge transfer transitions. TD-DFT calculations (Tables S3 and S4, ESI†) provide insights into electronic transitions, indicating redshifts in λ_{max}, with F^- causing the most prominent shift due to hydrogen bonding interaction and increased electron density on the nitrogen atom (Fig. S14a and b, ESI†). Fully functionalized **DHBBI-2-OH** showed negligible changes as the free N–H is not available. These findings enhance the understanding of **DHBBI** and F^- interactions. Fig. S15–S17 (ESI†) summarize the changes in emission intensity for the different analyte concentrations. The rapid drop in emission intensity was detected with a rise in F^- ion concentration. Fig. 5 demonstrates the variation of quenching activity while adding fixed (167 μM) concentrations of various anions. The F^- with **DHBBI** displayed the maximum selectivity and quenching efficiency.

The Stern–Volmer equation (K_{sv}) was employed to investigate the sensitivity of fluorescence quenching of **DHBBI** and its derivatives (eqn (1)). Fig. 6a displays the K_{sv} plot of the I_0/I change in response to different F^- ion analyte concentrations. In every case, the I_0/I value linearly increased with an increase in the concentration of the F^- ion. It is evident that the primary cause of the emission intensity decrease is the static quenching process. The calculated K_{sv} values are 11.6×10^4 M^{-1}, 8.86×10^4 M^{-1}, and 6.46×10^4 M^{-1} for **DHBBI**, **DHBBI-OH**, and **DHBBI-2-OH**. Among the synthesized molecules, **DHBBI** (K_{sv} = 11.6×10^4 M^{-1}) exhibits association rate constants towards the F^- ion that are approximately 1.30 and 1.80 times higher than that of **DHBBI-OH** (8.86×10^4 M^{-1}) and **DHBBI-2-OH** (6.46×10^4 M^{-1}), respectively. The larger K_{sv} values observed for **DHBBI** indicate efficient binding efficiency with TBAF analyte than other **DHBBI** derivatives (Fig. 6a and Fig. S18, S19, ESI†). Fig. 6b displays the K_{sv} data of **DHBBI** with different anionic analytes at various concentrations. The order of sensitivity for the various studied analytes is TBACN > TBAOH > $TBAClO_4$ > TBACl ≈ $TBANO_3$ > TBAI > TBABr > $TBAHSO_4$ > TBASCN for the

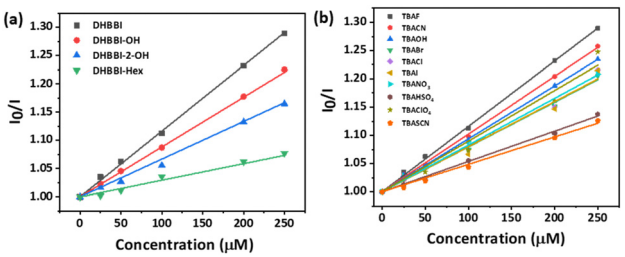

Fig. 6 (a) Variation in the Stern–Volmer (K_{sv}) plot of **DHBBI** and its derivatives treated with various concentrations of TBAF. (b) K_{sv} plot of **DHBBI** upon addition of different anions.

DHBBI molecule, according to Table S5 (ESI†), which summarizes the K_{sv} values. From Table S5 (ESI†), it is clear that **DHBBI** exhibits a maximum quenching rate constant compared to its other derivatives for TBAF. The decrease in emission intensity of **DHBBI** and **DHBBI-OH** is attributed to the free anthrapyrazolone N–H group in the core structure. Conversely, in **DHBBI-2-OH**, the anthrapyrazolone N–H group was functionalized by 2-bromoethanol, which did not efficiently interact with anions. This suggests that the free anthrapyrazolone N–H group in **DHBBI** and **DHBBI-OH** interacts with anions through hydrogen bonding. To understand the role of H bonding interactions of free OH functionality with anions, we have further investigated the emission behaviour with the model compound having hexyl alkyl chains (**DHBBI**-Hex). Testing of **DHBBI**-Hex with various anions did not show a response due to the absence of anthrapyrazolone N–H group (Fig. S20 and S21, ESI†) suggesting that free hydroxyl groups do not influence the hydrogen bonding interaction with anions. The strength of hydrogen bond formation for the anthrapyrazolone derivatives with F^- anions decreases in the order of **DHBBI** > **DHBBI-OH** > **DHBBI-2-OH** > **DHBBI**-Hex.

Hence, the interaction with anions is specifically due to the presence of the anthrapyrazolone N–H group in the designed molecules. Plotting of the emission intensities *versus* F^- concentration (Fig. S22, ESI†) helps in calculation of the LOD for **DHBBI**. The signal-to-noise ratio (SNR) was determined by calculating the final LODs using the formula LOD = $3.3 \times \sigma/m$, where σ is the standard deviation and m is the slope. 10.3 mM was determined to be the LOD for **DHBBI**.

To perform competitive fluorescence quenching, the **DHBBI**'s emission spectra were first measured. To achieve an efficient interaction, 150 μM of Cl^- was added to the solution and left to stabilize for 5 min. The addition of Cl^- anions caused no substantial change in the emission maximum of the solution. A solution containing F^- at a concentration of 150 μM was introduced into the solution, and the resultant emission spectrum was measured, revealing a substantial reduction in fluorescence intensity. The method of incorporating equal quantities of F^- and Cl^- ions was done multiple times, and the resulting emission spectra were also recorded. The same outcomes were also reported when other anions were employed instead of Cl^- (Fig. 7). The investigation demonstrates a reduction in the quenching efficiency, confirming the excellent selectivity of **DHBBI** for F^- ions even in the presence of other anionic analytes.

3.3. Sensing mechanism for F^- by DHBBI

To get more insight into the fluorescence emission quenching mechanism of **DHBBI** in the presence of F^- deep understanding is necessary. The fluorescence of the anthrapyrazolone group is exclusively explained by the intramolecular charge transfer (ICT) transition process. Fluorescence quenching was detected and the intensity of the intermolecular charge transfer transition was reduced upon the incorporation of an F^- anion. The presence of the –NH group in the **DHBBI** causes it to develop a hydrogen bond with the F^-. The excitation of **DHBBI**-F^- increases the efficiency of electron transfer and

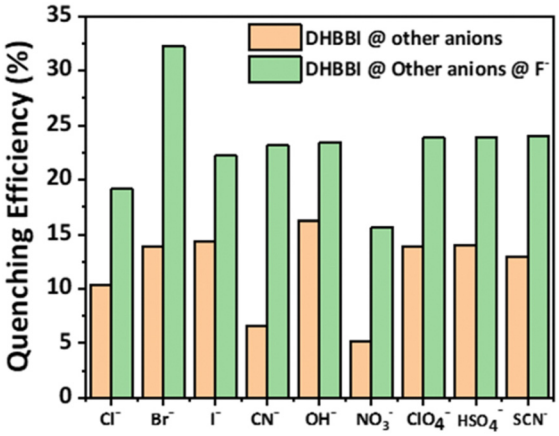

Fig. 7 Variation in the fluorescence quenching efficiency of **DHBBI** upon the addition of different anion analytes, followed by F^-.

internal conversion, which facilitates the nonradiative transition essential for the quenching of fluorescence. This effect can make the **DHBBI** a good candidate for sensing F^- anions (Fig. 8a). To further clarify the binding mechanism of F^- with **DHBBI**, analysis was performed by using FTIR (Fig. 8b). After the F^- ion binding with the **DHBBI**, the strong and sharp peak observed at 3023 cm^{-1} became weaker and shifted to a wavenumber of 2938 cm^{-1} due to the **DHBBI** and F^- interaction. Also, the small peak at 2857 cm^{-1} could be due to the N–H···F stretching after F^- binding. The FTIR spectra confirmed that the new peak at 2857 cm^{-1} is the N–H···F stretching after the

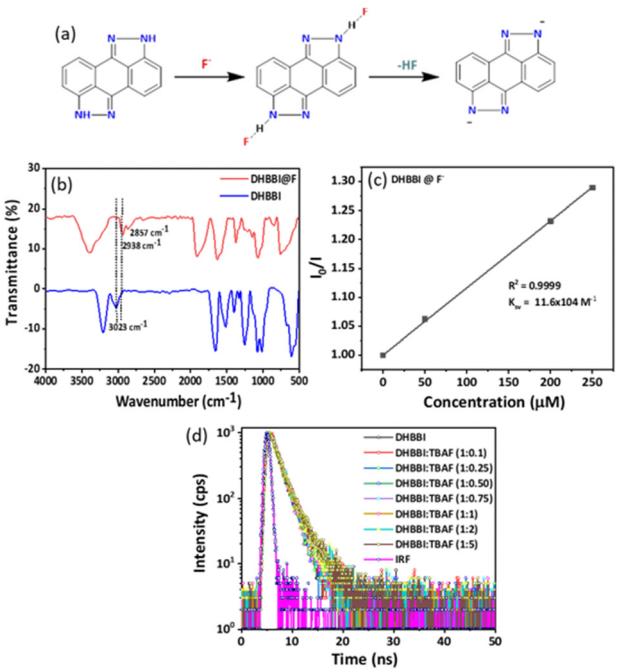

Fig. 8 (a) Plausible sensing mechanism for binding of **DHBBI** with F^- anions. (b) The binding mechanism of F^- with **DHBBI** analyzed by using FTIR. (c) Variation in the K_{sv} plot of **DHBBI** treated with different concentrations of F^-. (d) Change in the fluorescence decay of **DHBBI** (7×10^{-6} M) in ACN and treated with different concentrations of F^- at λ_{em} = 404 nm.

F^- binding through electrostatic interaction. Thus, F^- can have the capacity to bind with the **DHBBI** as a complex form.

The rapid quenching of **DHBBI** by F^- anions is due to the development of a significant charge transfer complex in the ground state, facilitated by ion pair electrostatic interactions. Based on the K_{sv} plot method (Fig. 8c and Table S6, ESI†), it can be shown that the variation in I_0/I in relation to the concentration of F^- follows a linear pattern. This indicates that the introduction of F^- causes the fluorescence to be statically quenched. To verify this procedure, we conducted fluorescence lifetime measurements for **DHBBI** both before and after the incorporation of different amounts of F^- anions. The fluorescence lifetime decay spectra and lifetime values exhibit minimal variation. This indicates that the quenching is a result of static quenching phenomena, as seen in Fig. 8d and Table S6 (ESI†). Thus, it can be confirmed that the presence of static quenching phenomena is the motive for the quenching process.

3.4. Comparison study

The fluorometric detection of F^- ions was investigated by using the **DHBBI** molecule and compared with previously reported probes used for the detection of F^- ions. The results, which are compiled in Table S7 (ESI†), demonstrate that the probes utilized in this investigation perform exceptionally well, having high binding constant, with high sensitivity, and selectivity towards F^-.

4. Conclusion

In conclusion, we have developed three anthrapyrazolone derivatives namely **DHBBI**, **DHBBI-OH**, and **DHBBI-2-OH** with an increase in the alkyl ethanol chains. The successful application of these derivatives as a fluorescence-based material for detecting F^- anions has been investigated. Fluorescence experiments demonstrated that, even in the presence of other competing anions, the selectivity and sensitivity for F^- ions were significantly higher in the case of **DHBBI** than that of other anthrapyrazolone derivatives. The outcomes of our research demonstrate that the **DHBBI** fluorescent molecule has a higher ability to reduce the fluorescence intensity owing to F^- ions, with a response that is $\sim$1.30 and 1.80 folds stronger compared to **DHBBI-OH** and **DHBBI-2-OH**. The **DHBBI** exhibited a higher Stern Volmer rate constant ($K_{sv} = 11.6 \times 10^4\ M^{-1}$), and LOD of 10.3 mM. The turn-off fluorescence behaviour is triggered by a static quenching mechanism involving intermolecular hydrogen bonding. The interference investigations with various anions have been explained to confirm the selectivity. Finally, DFT and TDDFT studies were employed for **DHBBI** and its derivatives to investigate their structural, photophysical, and electronic properties comprehensively, which validates the experimental results.

Author contributions

The manuscript was written through the contributions of all authors. All authors have approved the final version of the manuscript.

Data availability

The data used to support the findings of this study are included within the article.

Conflicts of interest

The authors declare no competing financial interest.

Acknowledgements

GS, AB and AD thank SRM IST for providing a fellowship to support the PhD program. SM acknowledged SRMIST for providing a seed grant and the Science and Engineering Research Board (SERB), India for a Core research grant (Project Code: CRG/2021/004203).

Notes and references

1 R. Martínez-Máñez and F. Sancenón, Fluorogenic and chromogenic chemosensors and reagents for anions, *Chem. Rev.*, 2003, **103**, 4419–4476.
2 Y. Zhou, Z. Xu and J. Yoon, Fluorescent and colorimetric chemosensors for detection of nucleotides, FAD and NADH: highlighted research during 2004–2010, *Chem. Soc. Rev.*, 2011, **40**, 2222.
3 M. Wenzel, J. R. Hiscock and P. A. Gale, Anion receptor chemistry: highlights from 2010, *Chem. Soc. Rev.*, 2012, **41**, 480–520.
4 R. M. Duke, E. B. Veale, F. M. Pfeffer, P. E. Kruger and T. Gunnlaugsson, Colorimetric, and fluorescent anion sensors: an overview of recent developments in the use of 1,8-naphthalimide-based chemosensors, *Chem. Soc. Rev.*, 2010, **39**, 3936.
5 A. F. Li, J. H. Wang, F. Wang and Y. B. Jiang, Anion complexation and sensing using modified urea and thiourea-based receptors, *Chem. Soc. Rev.*, 2010, **39**, 3729.
6 J. L. Sessler, D. G. Cho and V. Lynch, Diindolylquinoxalines: effective indole-based receptors for phosphate anion, *J. Am. Chem. Soc.*, 2006, **128**, 16518–16519.
7 M. J. Chmielewski, M. Charon and J. Jurczak, 1,8-Diamino-3,6-dichlorocarbazole: a promising building block for anion receptors, *Org. Lett.*, 2004, **6**, 3501–3504.
8 P. A. Gale, Anion receptor chemistry, *Chem. Commun.*, 2011, **47**, 82–86.
9 L. Wu, J. Liu, P. Li, B. Tang and T. D. James, Two-photon small-molecule fluorescence-based agents for sensing, imaging, and therapy within biological systems, *Chem. Soc. Rev.*, 2021, **50**, 702–734.
10 N. V. S. D. K. Bhupathiraju, W. Rizvi, J. D. Batteas and C. M. Drain, Fluorinated porphyrinoids as efficient platforms for new photonic materials, sensors, and therapeutics, *Org. Biomol. Chem.*, 2016, **14**, 389–408.
11 Y. Zheng, C. Tan, G. P. C. Drummen and Q. Wang, A luminescent lanthanide complex-based anion sensor with electron-donating methoxy groups for monitoring multiple

anions in environmental and biological processes, *Spectrochim. Acta, Part A*, 2012, **96**, 387–394.
12 M. K. Goshisht and N. Tripathi, Fluorescence-based sensors as an emerging tool for anion detection: mechanism, sensory materials and applications, *J. Mater. Chem. C*, 2021, **9**, 9820–9850.
13 S. Suganya, J. S. Park and S. Velmathi, Visual sensing of aqueous anions by C2-symmetric chemosensor and its application in real sample analysis, *Sens. Actuators, B*, 2014, **190**, 679–684.
14 X. Lou, D. Ou, Q. Li and Z. Li, An indirect approach for anion detection: the displacement strategy and its application, *Chem. Commun.*, 2012, **48**, 8462.
15 S. Mizukami, T. Nagano, Y. Urano, A. Odani and K. Kikuchi, A fluorescent anion sensor that works in neutral aqueous solution for bioanalytical application, *J. Am. Chem. Soc.*, 2002, **124**, 3920–3925.
16 C. Sonkar, S. Sarkar, N. Malviya, M. L. Kuznetsov and S. Mukhopadhyay, Recognition and mechanistic investigation of anion sensing by ruthenium arene complexes and bioimaging application, *Dalton Trans.*, 2022, **51**, 13071–13084.
17 G. Picci, R. Montis, A. M. Gilchrist, P. A. Gale and C. Caltagirone, Fluorescent and colorimetric sensors for anions: highlights from 2020 to 2022, *Coord. Chem. Rev.*, 2024, **501**, 215561.
18 B. Bhattacharyya, A. Kundu, N. Guchhait and K. Dhara, Anthraimidazoledione based reversible and reusable selective chemosensors for fluoride ion: Naked-eye, colorimetric and fluorescence "ON–OFF", *J. Fluoresc.*, 2017, **27**, 1041–1049.
19 D. Singhal, N. Gupta and A. K. Singh, The anion recognition properties of a novel hydrazone based on colorimetric and potentiometric studies, *Mater. Sci. Eng., C*, 2016, **58**, 548–557.
20 E. Saikia, M. P. Borpuzari, B. Chetia and R. Kar, Experimental and theoretical study of urea and thiourea based new colorimetric chemosensor for fluoride and acetate ions, *Spectrochim. Acta, Part A*, 2016, **152**, 101–108.
21 R. Hein, P. D. Beer and J. J. Davis, Electrochemical anion sensing: supramolecular approaches, *Chem. Rev.*, 2020, **120**, 1888–1935.
22 P. Doble and P. R. Haddad, Indirect photometric detection of anions in capillary electrophoresis, *J. Chromatogr. A*, 1999, **834**, 189–212.
23 S. B. Butt and M. Riaz, Determination of cations and anions in environmental samples by HPLC: review, *J. Liq. Chromatogr. Relat. Technol.*, 2009, **32**, 1045–1064.
24 D. Y. Lee, N. Singh and D. O. Jang, A benzimidazole-based single molecular multianalyte fluorescent probe for the simultaneous analysis of Cu^{2+} and Fe^{3+}, *Tetrahedron Lett.*, 2010, **51**, 1103–1106.
25 N. Kaur and S. Kumar, Single molecular colorimetric probe for simultaneous estimation of Cu^{2+} and Ni^{2+}, *Chem. Commun.*, 2007, 3069.
26 M. Schmittel and H. W. Lin, Quadruple-channel sensing: a molecular sensor with a single type of receptor site for selective and quantitative multi-Ion analysis, *Angew. Chemie.*, 2007, **119**, 911–914.
27 J.-M. You, H. Jeong, H. Seo and S. Jeon, A new fluoride ion colorimetric sensor based on dipyrrolemethanes, *Sens. Actuators, B*, 2010, **146**, 160–164.
28 D. A. Jose, D. K. Kumar, B. Ganguly and A. Das, Efficient and simple colorimetric fluoride ion sensor based on receptors having urea and thiourea binding sites, *Org. Lett.*, 2004, **6**, 3445–3448.
29 V. K. Harikrishnan, S. M. Basheer, N. Joseph and A. Sreekanth, Colorimetric and fluorimetric response of salicylaldehyde dithiosemicarbazone towards fluoride, cyanide and copper ions: spectroscopic and TD-DFT studies, *Spectrochim. Acta, Part A*, 2017, **182**, 160–167.
30 G. Y. Li, D. Liu, H. Zhang, W. W. Li, F. Wang and Y. H. Liang, TDDFT study on the sensing mechanism of a fluorescent sensor for fluoride anion: inhibition of the ESPT process, *Spectrochim. Acta, Part A*, 2015, **149**, 17–22.
31 C. P. Carvalho, R. Ferreira, J. P. Da Silva and U. Pischel, An aminonaphthalimide–putrescine conjugate as fluorescent probe for cucurbituril host–guest complexes, *Supramol. Chem.*, 2013, **25**, 92–100.
32 A. A. Kumaran, A. Chithrambattu, B. Vedhanarayanan, S. B. A. Rajukrishnan, V. K. Praveen and R. N. Kizhakayil, Fluoride-philic reduced graphene oxide–fluorophore anion sensors, *Mater. Adv.*, 2022, **3**, 6809–6817.
33 S. Peckham and N. Awofeso, Water Fluoridation: A Critical Review of the Physiological Effects of Ingested Fluoride as a Public Health Intervention, *Sci. World J.*, 2014, **2014**, 1–10.
34 A. K. Mascarenhas and B. A. Burt, Fluorosis risk from early exposure to fluoride toothpaste, *Community Dent. Oral Epidemiol.*, 1998, **26**, 241–248.
35 H. Matsui, M. Morimoto, K. Horimoto and Y. Nishimura, Some characteristics of fluoride-induced cell death in rat thymocytes: cytotoxicity of sodium fluoride, *Toxicol. In Vitro*, 2007, **21**, 1113–1120.
36 D. E. Gross, V. Mikkilineni, V. M. Lynch and J. L. Sessler, Bis-amidopyrrolyl receptors based on anthracene and carbazole, *Supramol. Chem.*, 2010, **22**, 135–141.
37 G. Singh, Pawan, Mohit, Sushma, B. Singh, D. González-Silverac, C. Espinosa-Ruízc, M. A. Estebanc and A. Kaur, Anthracene-based triazolyl triethoxysilanes as selective and colorimetric sensor for cysteine: rationalization towards stability factors, therapeutics evaluation and molecular docking, *ChemistrySelect*, 2021, **6**, 8899–8911.
38 N. Wanichacheva, S. Watpathomsub, V. S. Lee and K. Grudpan, Synthesis of a novel fluorescent sensor bearing dansyl fluorophores for the highly selective detection of Mercury(II) ions, *Molecules*, 2010, **15**, 1798–1810.
39 J. B. Chae, D. Yun, H. Lee, H. Lee, K.-T. Kim and C. Kim, Highly sensitive dansyl-based chemosensor for detection of Cu^{2+} in aqueous solution and Zebrafish, *ACS Omega*, 2019, **4**, 12537–12543.
40 M. H. Mahnashi, A. M. Mahmoud, S. A. Alkahtani, R. Ali and M. M. El-Wekil, A novel imidazole derived colorimetric and fluorometric chemosensor for bifunctional detection of copper(II) and sulphide ions in environmental water samples, *Spectrochim. Acta, Part A*, 2020, **228**, 117846.

41 S. Manoj Kumar, D. Jothi, S. Munusamy, S. Enbanathan and S. Kulathu Iyer, Imidazole-derived new colorimetric/fluorometric chemosensor for the sensitive recognition of CN^- ions: real-time application in food samples and fluorescence bio-imaging, *J. Photochem. Photobiol., A*, 2023, **434**, 114269.
42 G. Kumar, N. Gupta, K. Paul and V. Luxami, Acrylonitrile embedded benzimidazole-anthraquinone based chromofluorescent sensor for ratiometric detection of CN^- ions in bovine serum albumin, *Sens. Actuators, B*, 2018, **267**, 549–558.
43 L. Hou, X. Kong, Y. Wang, J. Chao, C. Li, C. Dong, Y. Wang and S. Shuang, An anthraquinone-based highly selective colorimetric and fluorometric sensor for sequential detection of Cu^{2+} and S^{2-} with intracellular application, *J. Mater. Chem. B*, 2017, **5**, 8957–8966.
44 G. W. Lee, N.-K. Kim and K.-S. Jeong, Synthesis of biindole−diazo conjugates as a colorimetric anion receptor, *Org. Lett.*, 2010, **12**, 2634–2637.
45 K. Karuppiah, H. Muniyasamy, M. Sepperumal and S. Ayyanar, Design and synthesis of new salicylhydrazone tagged indole derivative for fluorometric sensing of Zn^{2+} ion and colorimetric sensing of F^- ion: applications in live cell imaging, *Microchem. J.*, 2020, **159**, 105543.
46 P. Madhusudhana Reddy, S. R. Hsieh, J. K. Chen, C. J. Chang, J. Y. Kang and C. H. Chen, Robust, sensitive and facile method for detection of F^-, CN^- and Ac^- anions, *Spectrochim. Acta, Part A*, 2017, **186**, 8–16.
47 A. E. Prestiani and B. Purwono, Styrene and azo-styrene based colorimetric sensors for highly selective detection of cyanide, *Indones. J. Chem.*, 2017, **17**, 238.
48 F. Wang, L. Wang, X. Chen and J. Yoon, Recent progress in the development of fluorometric and colorimetric chemosensors for detection of cyanide ions, *Chem. Soc. Rev.*, 2014, **43**, 4312.
49 P. Yadav, H. Laddha, M. Agarwal and R. Gupta, Colorimetric assay of fluoride goes digital: on the spot testing of F^- ions in water using smartphone's digital imaging and test strip assay by a novel chromofluorogenic receptor based on 1,8-naphthalimide, *J. Mol. Liq.*, 2021, **324**, 114690.
50 M. Li, X. Li, M. Jiang, X. Liu, Z. Chen, S. Wang, T. D. James, L. Wang and H. Xiao, Engineering a ratiometric fluorescent sensor membrane containing carbon dots for efficient fluoride detection and removal, *Chem. Eng. J.*, 2020, **399**, 125741.
51 N. Wu, L.-X. Zhao, C.-Y. Jiang, P. Li, Y. Liu, Y. Fu and F. Ye, A naked-eye visible colorimetric and fluorescent chemosensor for rapid detection of fluoride anions: implication for toxic fluorine-containing pesticides detection, *J. Mol. Liq.*, 2020, **302**, 112549.
52 K. Durga Prasad, N. Venkataramaiah and T. N. Guru Row, 1,9-Pyrazoloanthrone as a colorimetric and ''Turn-On'' fluorometric chemosensor: structural implications, *Cryst. Growth Des.*, 2014, **14**, 2118–2122.
53 S. Saravanan, R. Ahmad, S. Kasthuri, K. Pal, S. Raviteja, P. Nagaraaj, R. Hoogenboom, V. Nutalapati and S. Maji, Pyrazoloanthrone-functionalized fluorescent copolymer for the detection and rapid analysis of nitroaromatics, *Mater. Chem. Front.*, 2021, **5**, 238–248.
54 S. Saravanan, T. M. Sheeba Rani, A. Deepak Nazare, V. Nutalapati and S. Maji, Fluorometric detection of fluoride and thiocyanate ions using novel anthrapyrazolone derivatives, *Mater. Today: Proc.*, 2021, **40**, S241–S247.
55 M. A. Naik, N. Venkatramaiah, C. Kanimozhi and S. Patil, Influence of side-chain on structural order and photophysical properties in thiophene based diketopyrrolopyrroles: a systematic study, *J. Phys. Chem. C*, 2012, **116**, 26128–26137.